High-resolution tomography for galaxy spectroscopic surveys with angular redshift fluctuations

L. Legrand[1], C. Hernández-Monteagudo[2], M. Douspis[1], N. Aghanim[1], and Raúl E. Angulo[3, 4]

[1] Université Paris-Saclay, CNRS, Institut d'astrophysique spatiale, 91405, Orsay, France.
  e-mail: louis.legrand@outlook.com
[2] Centro de Estudios de Física del Cosmos de Aragón (CEFCA), Unidad Asociada al CSIC, Plaza San Juan, 1, planta 2, E-44001, Teruel, Spain
[3] Donostia International Physics Centre (DIPC), Paseo Manuel de Lardizabal 4, E-20018 Donostia-San Sebastian, Spain
[4] IKERBASQUE, Basque Foundation for Science, E-48013, Bilbao, Spain

February 24, 2021

ABSTRACT

In the context of next-generation spectroscopic galaxy surveys, new statistics of the distribution of matter are currently being developed. Among these, we investigated the angular redshift fluctuations (ARF), which probe the information contained in the projected redshift distribution of galaxies. Relying on the Fisher formalism, we show how ARF will provide complementary cosmological information compared to traditional angular galaxy clustering. We tested both the standard ΛCDM model and the wCDM extension. We find that the cosmological and galaxy bias parameters express different degeneracies when inferred from ARF or from angular galaxy clustering. As such, combining both observables breaks these degeneracies and greatly decreases the marginalised uncertainties by a factor of at least two on most parameters for the ΛCDM and wCDM models. We find that the ARF combined with angular galaxy clustering provide a great way to probe dark energy by increasing the figure of merit of the w_0-w_a parameter set by a factor of more than ten compared to angular galaxy clustering alone. Finally, we compared ARF to the CMB lensing constraints on the galaxy bias parameters. We show that a joint analysis of ARF and angular galaxy clustering improves constraints by ∼ 40% on galaxy bias compared to a joint analysis of angular galaxy clustering and CMB lensing.

Key words. Cosmology: large-scale structure of Universe - observations - cosmological parameters - dark energy

1. Introduction

In the coming years, large-scale optical and infrared (IR) surveys will map our Universe from the present epoch up to when it was roughly one tenth of its current age with unprecedented accuracy. A significant part of these surveys will be spectroscopic; for example, DESI (DESI Collaboration et al. 2016), 4MOST (de Jong & 4MOST Consortium 2015), WEAVE (Bonifacio et al. 2016), and NISP aboard *Euclid* (Laureijs et al. 2011), and they will provide us with spectra for large samples of sources. Such spectra will not only enable deep insight into the physics of those objects, but it will also yield accurate estimates of their redshift and thus of their distance to the observer. From the cosmological point of view, this will enable a precise (statistical) characterisation of the (apparent) spatial distribution of those luminous tracers (via two- or three-point statistics), and this itself should shed precious light on open topics such as the nature of dark energy, the possible interplay of dark energy and dark matter, the mass hierarchy of neutrinos, or possible deviations of gravity from general relativity, to name a few.

At the same time, a different family of surveys will scan the sky at greater depths with optical filters and exquisite image quality. These photometric experiments build very large and high-quality source catalogues, with, however, relatively rough redshift estimations given their moderate number of filters. While mining the faint Universe, these types of surveys will be particularly sensitive, from a cosmological perspective, to the angular clustering of luminous matter, the cosmological aspects

of gravitational lensing throughout cosmic epochs, the satellite population in halos, and the formation and evolution of the population of galaxy clusters. In this context, the Dark Energy Survey (DES, Abbott et al. 2018) is currently providing state-of-the-art cosmological constraints in the late universe, and these should be further complemented by the Vera Rubin Observatory (LSST, Ivezić et al. 2019), which, at the same time, will also explore the variability of the night sky in a regime of depth and time domain that remains practically unexplored to date.

An intermediate, third class of experiments also exists. These are the spectro-photometric surveys that conduct standard photometry in a relatively large set (from ∼ 10 up to ∼ 60) of narrow-band optical filters. This strategy combines the indiscriminate character of the photometric surveys with *high* precision redshift estimates ($\Delta z/(1 + z) \sim 10^{-3}$–$10^{-2}$) for a large fraction (> 20–30 %) of the detected sources. Given its multi-colour character, these surveys are able to provide pseudo- and photospectra in each pixel of the surveyed area. The pioneer example of COMBO-17 has been or is being followed by other efforts such as COSMOS (Scoville et al. 2007), ALHAMBRA (Moles et al. 2008), SHARDS (Pérez-González et al. 2013), PAU (Martí et al. 2014), J-PAS (Benitez et al. 2014), SPHEREx (Doré et al. 2014), and J-PLUS (Cenarro et al. 2019).

In this work, we forecast the cosmological constraints for upcoming spectroscopic and spectro-photometric surveys. In these types of surveys, it is customary to convert redshift estimates into radial distances under the assumption of a given fiducial cosmological model. Angular and redshift coordinates are thus

converted into 3D space, where standard 3D clustering analysis techniques are applied.

In our case, however, we chose to follow a different strategy. We focused on a new cosmological observable, namely the angular redshift fluctuations (ARF; Hernández-Monteagudo et al. 2019 hereafter HMCMA). Being a 2D observable, the ARF field can easily be cross-correlated with other 2D observables, such as the 2D galaxy density filed and the CMB lensing fields. As shown in HMCMA, ARF are sensitive to the variation of matter density and velocity along the line of sight, while galaxy density is sensitive to the the average or monopole of matter density and velocity in the same redshift range. ARF present other interesting features, such as being correlated to the cosmic, radial, peculiar velocity fields, or being particularly insensitive to additive systematics that remain constant under the redshift shell subject to analysis (HMCMA; Chaves-Montero et al. 2019).

In this work, we applied the Fisher formalism to the angular galaxy clustering, the ARF, and the CMB lensing convergence observables, and we explored their sensitivity to cosmology in two different observational setups, mimicking those expected for the DESI and *Euclid* surveys. We considered the CMB lensing convergence field among our observables, since it constitutes an intrinsically different probe, of which the dependence on the parameters defining the galaxy sample is different from that of angular galaxy clustering and ARF. Our scope is to assess whether the ARF field can provide complementary information on the galaxy density field and on the CMB lensing field.

The paper is organised as follows. We introduce the spectroscopic galaxy surveys and CMB experiments that we used in our analysis in Sect. 2. In Sect. 3, we present the angular galaxy clustering, the ARF, and the CMB lensing convergence field. In Sect. 4, we compute the foreseen signal-to-noise ratios of these probe combinations, whilst also introducing the covariance among those observables. In Sect. 5, we present the predicted constraints on cosmological parameters in the fiducial ΛCDM scenario. Finally, we discuss our findings in Sect. 6 and conclude in Sect. 7.

Throughout this paper, we use the *Planck* 2018 cosmology as our fiducial cosmology. We take the values given in Table 2, column 6 (best-fit with BAO) of Planck Collaboration et al. (2020a). We use the following naming conventions: *observable* refers to a spherical 2D field built on measured quantities such as counts, redshifts, or deflection angles, while *probe* refers to the combination of one or two observables in a given set of summary statistics. In practice, our probes will be the two-point angular power spectra C_ℓ. The redshift due to the Hubble expansion is denoted by z, while $z_{\rm obs}$ is the measured redshift (which includes redshift distortions induced by radial peculiar velocities). $\Omega_{\rm m,0}$ is the density of matter at $z = 0$ in units of the critical density, and H_0 is the Hubble constant. $r(z) = \int \mathrm{d}z\, c\, /\, H(z)$ is the line of sight comoving distance, and $\mathrm{d}V_\Omega = \mathrm{d}V/\mathrm{d}\Omega = r^2\, \mathrm{d}r = r^2(z)\, c/H(z)\, \mathrm{d}z$ is the comoving volume element per solid angle, with $\mathrm{d}\Omega$ being a differential solid angle element. Vectors are in bold font, and a hat denotes a unit vector.

2. Surveys

Among the wealth of current and upcoming experiments, we chose two representative cases for spectroscopic large scale structure (LSS) surveys, namely the DESI and the *Euclid* experiments. We detail their specifications in Table 1.

Concerning the CMB, we first considered a *Planck*-like experiment, which is currently a state-of-the-art database in terms

of multi-frequency, full sky CMB data (Planck Collaboration et al. 2020a). In order to observe the future sensitivity reachable on the smallest angular scales via ground CMB experiments, we also considered the Simons Observatory (The Simons Observatory Collaboration et al. 2019) and the CMB Stage 4 (Abazajian et al. 2019). Both cover thousands of square degrees of the southern sky (> 40% of the sky) with extremely high sensitivity (≤ 2 μK arcmin) and fine angular resolution (at the arcmin level).

2.1. The DESI experiment

In this section, we discuss DESI, which is a ground-based survey that will cover $14,000\ {\rm deg}^2$ on the sky and will measure the redshift of about 30 million galaxies using optical-fibre spectroscopy (DESI Collaboration et al. 2016). It will target four different classes of galaxies. In this work, we computed forecasts for the emission line galaxy (ELG) sample, which is the largest sample of the survey. It ranges from $z = 0.6$ up to $z = 1.6$. The expected galaxy distribution $\bar{n}_{\rm g}(z)$ (see Fig. 1a) and the galaxy bias $b(z)$ are calibrated based on the DEEP2 survey (Newman et al. 2013). The uneven shape of the redshift distribution of galaxies can be explained by the selection effect of the DESI survey and by the sample variance in the DEEP2 survey. The (linear) bias of the spatial distribution of this galaxy population with respect to dark matter is a redshift-dependent quantity approximated by

$$b_{\rm g}(z) = 0.84/D(z)\,, \tag{1}$$

with $D(z)$ denoting the growth factor of linear matter density perturbations.

2.2. The Euclid spectroscopic survey

The *Euclid* satellite will observe about $15\,000\ {\rm deg}^2$ of the extragalactic sky (Laureijs et al. 2011). The NISP instruments will provide slitless spectroscopy, allowing for precise redshift determinations for about 1950 gal deg^{-2}. The spectroscopic survey will target H$_\alpha$ emission-line galaxies in the redshift range $0.9 < z < 1.8$. We assumed model 3 from Pozzetti et al. (2016) for the expected number density of galaxies $\bar{n}_{\rm g}(z)$ (see Fig. 1b). For the expected galaxy linear bias, we fit a linearly redshift dependent bias on the values of the Table 3 of Euclid Collaboration et al. (2020), yielding

$$b_{\rm g}(z) = 0.79 + 0.68\,z\,. \tag{2}$$

2.3. Tomography

As already mentioned above, our forecasts are based on a tomographic approach where the entire redshift range covered by a galaxy survey is sliced into different redshift bins. Centred at each of these redshift bins, we considered Gaussian redshift shells of a given width $\sigma_{\rm z}$ centred on redshifts z_i:

$$W_i(z) = \exp\left(-\frac{(z - z_i)^2}{2\sigma_{\rm z}^2}\right)\,. \tag{3}$$

Provided that a Gaussian shell dilutes information on radial scales shorter than the Gaussian width, our choice of $\sigma_{\rm z}$ is a compromise between maximising the amount of radial scales under study, and minimising the impact of non-linear, radial scales in the analysis (Asorey et al. 2012; Di Dio et al. 2014). In HMCMA, we find that, at $z \simeq 1$, down to $\sigma_{\rm z} = 0.01$, the impact of radial non-linearities is either negligible or easily tractable with

Survey	*Euclid*	DESI
Survey area	15 000 deg^2	14 000 deg^2
Redshift estimation	Slitless spectroscopy	Optical fibre spectroscopy
Targets	H_α emission line	[OII] doublet
Redshift range	$0.9 < z < 1.8$	$0.6 < z < 1.6$
Average number of galaxies	1950 gal deg^{-2}	1220 gal deg^{-2}
Galaxy bias	$b_{\rm g}(z) = 0.79 + 0.68\,z$	$b_{\rm g}(z) = 0.84/D(z)$
Reference	Euclid Collaboration et al. (2020)	DESI Collaboration et al. (2016)

Table 1: Specifications for the two galaxy surveys under consideration.
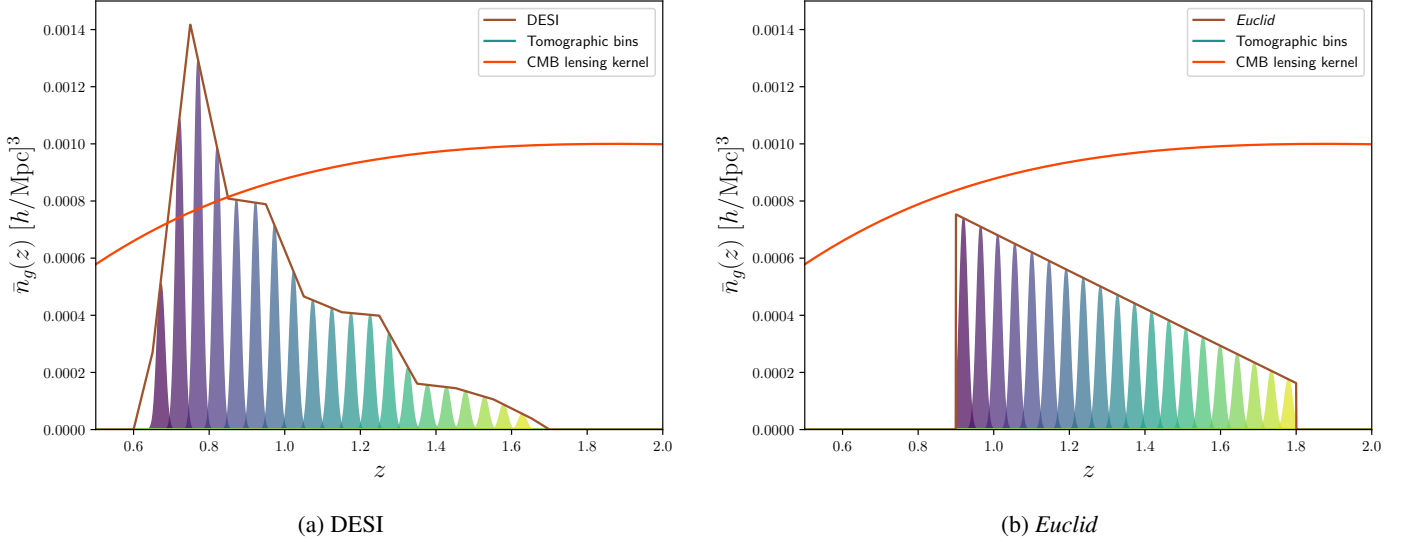

(a) DESI

(b) *Euclid*

Fig. 1: Galaxy density distribution as a function of redshift for the emission line galaxies (ELG) of DESI (left panel), and the *Euclid* spectroscopic sample (right panel). The filled coloured lines show the Gaussian bins used in our analysis, colour-coded as a function of the bin index. The orange line shows the CMB lensing efficiency kernel (with arbitrary normalisation).

a Gaussian kernel describing thermal, stochastic, radial motions. We thus adopted $\sigma_{\rm z} = 0.01$ for our forecasts.

As shown in Asorey et al. (2012), the angular galaxy clustering analysis can recover the same amount of information as the 3D analysis when the bin size is comparable to the maximum scale probed by the 3D analysis. This gives $\sigma_{\rm z} c/H(z) \simeq 2\pi/k_{\rm max}$, so in our case, for $z = 1$ and $k_{\rm max} = 0.2\ h\ {\rm Mpc}^{-1}$ (see Sect. 3), we obtain $\sigma_{\rm z} \simeq 0.01$, corresponding to our choice of bin size.

For each of the two galaxy surveys under consideration, we took 20 redshift bins, and since the overlap between consecutive bins is not zero, we account for all cross-correlations between shells in the covariance matrix. In this way, redundant information between different shells is fully accounted for. The redshift bins sample the range from $z = 0.65$ to $z = 1.65$ for DESI, and from $z = 0.9$ to $z = 1.8$ for *Euclid*. These redshift bins are displayed in Figs. 1a and 1b, together with the expected number density of tracers for each survey.

2.4. The Planck experiment

The *Planck* satellite was launched in 2009 and scanned the full sky until 2013 in CMB frequencies. The satellite hosted two instruments, the HFI operating in six frequency bands between 100 GHz and 857 GHz, and the LFI instrument operating in three bands between 30 GHz and 77 GHz. The CMB maps were produced by combining these frequencies to remove the contribution from the galaxy and other foreground sources. The final

maps have noise of $27\,\mu K$ arcmin, and an effective beam with a full width at half maximum of 7 arcmin. The final data release of *Planck* was published in Planck Collaboration et al. (2020a).

The CMB lensing field has been estimated with a minimum variance quadratic estimator, combining temperature and polarisation data. It is to date the most precise map of the integral of the density of matter on the full extra galactic sky, covering $\sim 70\,\%$ of the sky, which made it possible to obtain an estimate of the lensing-potential power spectrum over lensing multipoles $8 \le L \le 400$ (Planck Collaboration et al. 2020b).

2.5. The Simons Observatory

The Simons Observatory consists of four different telescopes placed in the Atacama desert in Chile, with the goal of providing an exquisite mapping of the CMB intensity and polarisation anisotropies from a few degrees down to arcminute scales. Three of the telescopes have 0.5 m of aperture, and with an angular resolution close to half a degree, map 10 % of the sky targeting the moderate-to-large angular scales. Their primary goal is to measure large-scale polarisation from the background of primordial gravitational waves.

Alongside these small telescopes, one 6 m diameter telescope will observe at 27, 39, 93, 145, 225, and 280 GHz, with an angular resolution close to the arcminute, which is necessary to obtain a high-resolution map of the lensing potential of the

CMB. It is expected to reach a sensitivity level of 6 μK arcmin on 40 % of the sky.

2.6. CMB Stage 4

The CMB Stage 4 (CMB-S4) experiment will be the successor of the Simons Observatory and will combine resources with the successor of the South Pole telescope and the BICEP/Keck collaborations. Its main scope is to measure the imprint of primordial gravitational waves on the CMB polarisation anisotropy, but it will also perform a wide survey with a high resolution that will allow us to probe the secondary anisotropies with unprecedented accuracy. Its deep and wide survey will cover $\sim$ 60% of the extragalactic sky and will be conducted over seven years using two 6 m telescopes located in Chile, each equipped with $121,760$ detectors distributed over eight frequency bands from 30 GHz to 270 GHz. These observations will provide CMB temperature and polarisation maps with a resolution of ≤ 1.5 arcmin and with a noise level of 1 μK arcmin. This very high sensitivity at small scales both in temperature and polarisation, on a large fraction of the sky, will ensure an accurate estimation of the CMB lensing potential.

3. Observables

In this paper, we consider three different observables, namely the angular galaxy clustering, the corresponding ARF, and the CMB lensing convergence field. In order to compute the forecasts, we restricted our study to the linear scales, where the cosmological linear theory of perturbations apply. In practice, we ignored all scales above $k_{\max} = 0.2\,h\,\mathrm{Mpc}^{-1}$ at all redshifts. This is a conservative approach, as one could consider a scale cutoff that evolves with redshift as in Di Dio et al. (2014). We also assumed that our observables were Gaussian distributed, and that the information content was completely captured by the two-point momenta, and in particular the angular power spectrum, either auto or cross, depending on whether we combined different observables or not. In what follows, we describe our model of the observables, so that expressions for their angular power spectrum can be derived thereafter.

3.1. Galaxy angular density fluctuations

The 3D field of the number density of galaxies is noted as $n_{\mathrm{g}}(z, \hat{\boldsymbol{n}})$, where $\hat{\boldsymbol{n}}$ denotes a direction on the sky. The average number density of galaxies at a redshift z is defined by $\bar{n}_{\mathrm{g}}(z) = \left\langle n_{\mathrm{g}}(z, \hat{\boldsymbol{n}}) \right\rangle_{\hat{\boldsymbol{n}}}$. The 3D field of galaxy density contrast is then given by

$$\delta_{\mathrm{g}}^{\mathrm{3D}}(z, \hat{\boldsymbol{n}}) = \frac{n_{\mathrm{g}}(z, \hat{\boldsymbol{n}}) - \bar{n}_{\mathrm{g}}(z)}{\bar{n}_{\mathrm{g}}(z)} \ . \tag{4}$$

We assume that the galaxy density contrast traces the dark matter density contrast $\delta_{\mathrm{m}}^{\mathrm{3D}}$ via a scale-independent bias: $\delta_{\mathrm{g}}^{\mathrm{3D}}(z, \hat{\boldsymbol{n}}) = b_{\mathrm{g}}(z)\,\delta_{m}^{\mathrm{3D}}(z, \hat{\boldsymbol{n}})$. This bias depends on the properties of the galaxies used as a tracer for each survey, and they are given in Eqs. 1 and 2.

In our analysis, we modelled the observed redshift of galaxies z_{obs} as a 3D field. It is defined as the sum of the redshift induced by the Hubble flow, and the redshift due to the peculiar velocity of galaxies:

$$z_{\mathrm{obs}}(z, \hat{\boldsymbol{n}}) = z + (1 + z)\frac{\mathbf{v}(z, \hat{\boldsymbol{n}}) \cdot \hat{\boldsymbol{n}}}{c} \ , \tag{5}$$

where $\mathbf{v}$ is the peculiar velocity field of galaxies. We neglect other sources of redshift distortions that are significantly smaller than those considered here (HMCMA).

The angular galaxy clustering field is then modelled by an integral along the line of sight in which, at every redshift z, only galaxies within the selection function $W(z_{\mathrm{obs}}; z_i)$ are included:

$$\delta_{\mathrm{g}}^i(\hat{\boldsymbol{n}}) = \frac{1}{N_{\mathrm{g}}^i} \int_{z=0}^{\infty} \mathrm{d}V_\Omega\, \bar{n}_{\mathrm{g}}(z)\, b_{\mathrm{g}}(z)\, \delta_{\mathrm{m}}^{\mathrm{3D}}(z, \hat{\boldsymbol{n}})\, W_i\left[z_{\mathrm{obs}}(z, \hat{\boldsymbol{n}})\right], \tag{6}$$

where $N_{\mathrm{g}}^i = \int_{z=0}^{\infty} \mathrm{d}V_\Omega\, \bar{n}_{\mathrm{g}}(z)\, W_i(z)$ is the average number of galaxies per solid angle, under the i-th selection function W_i centred on redshift z_i, and in practice can be computed from an angular average over the survey's footprint.

We next expand the selection function, retaining only linear terms in density and velocity fluctuations, finding the following:

$$\delta_{\mathrm{g}}^i(\hat{\boldsymbol{n}}) \simeq \frac{1}{N_{\mathrm{g}}^i} \int_{z=0}^{\infty} \mathrm{d}V_\Omega\, \bar{n}_{\mathrm{g}}(z)\, W_i(z)$$
$$\times \left[b_{\mathrm{g}}(z)\, \delta_{\mathrm{m}}^{\mathrm{3D}}(z, \hat{\boldsymbol{n}}) + (1 + z)\frac{\mathrm{d}\ln W_i}{\mathrm{d}z}\frac{\mathbf{v}(z, \hat{\boldsymbol{n}}) \cdot \hat{\boldsymbol{n}}}{c} \right], \tag{7}$$

with the derivative $\mathrm{d}\ln W_i/\mathrm{d}z = -(z - z_i)/\sigma_{\mathrm{z}}^2$.

3.2. Angular redshift fluctuations

The ARF field represents the spatial variations of the average redshift of galaxies on the sky. The average redshift of galaxies is given by

$$\bar{z} = \frac{1}{N_{\mathrm{g}}^i} \left\langle \int_{z=0}^{\infty} \mathrm{d}V_\Omega\, z_{\mathrm{obs}}(z, \hat{\boldsymbol{n}})\, n_{\mathrm{g}}(z, \hat{\boldsymbol{n}})\, W_i\left[z_{\mathrm{obs}}(z, \hat{\boldsymbol{n}})\right] \right\rangle_{\hat{\boldsymbol{n}}}$$
$$= \frac{1}{N_{\mathrm{g}}^i} \int_{z=0}^{\infty} \mathrm{d}V_\Omega\, z\, \bar{n}_{\mathrm{g}}(z)\, W_i(z) \ . \tag{8}$$

We thus define the ARF field as follows:

$$\delta_{\mathrm{z}}^i(\hat{\boldsymbol{n}}) = \frac{1}{N_{\mathrm{g}}^i} \int_{z=0}^{\infty} \mathrm{d}V_\Omega\, (z_{\mathrm{obs}}(z, \hat{\boldsymbol{n}}) - \bar{z})\, \bar{n}_{\mathrm{g}}(z)$$
$$\times \left[1 + b_{\mathrm{g}}(z)\, \delta_{\mathrm{m}}^{\mathrm{3D}}(z, \hat{\boldsymbol{n}}) \right] W_i\left[z_{\mathrm{obs}}(z, \hat{\boldsymbol{n}})\right] \ , \tag{9}$$

where we again refer to a redshift bin centred upon z_i. Expanding the Gaussian selection function at first order and retaining only linear terms in density and velocity, we find

$$\delta_{\mathrm{z}}^i(\hat{\boldsymbol{n}}) \simeq \frac{1}{N_{\mathrm{g}}^i} \int_{z=0}^{\infty} \mathrm{d}V_\Omega\, \bar{n}_{\mathrm{g}}(z)\, W_i(z) \left[(z - \bar{z})\, b_{\mathrm{g}}(z)\, \delta_{\mathrm{m}}^{\mathrm{3D}}(z, \hat{\boldsymbol{n}}) \right.$$
$$\left. + (1 + z)\frac{\mathbf{v}(z, \hat{\boldsymbol{n}}) \cdot \hat{\boldsymbol{n}}}{c}\left(1 + (z - \bar{z})\frac{\mathrm{d}\ln W_i}{\mathrm{d}z} \right) \right]. \tag{10}$$

We note that given the small widths adopted ($\sigma_{\mathrm{z}} = 0.01$), it is safe to assume that the bias $b(z)$ remains constant within the redshift bin.

3.3. CMB lensing

The image of the primary CMB, emitted at the moment of recombination at $z \simeq 1100$, is distorted by the gravitational lensing arising as a consequence of the (slightly inhomogeneous) mass distribution between us and the surface of the last scattering. This modifies the initial anisotropy pattern and creates

statistical anisotropy (see Lewis & Challinor 2006 for a review). Assuming that the primordial CMB is Gaussian and statistically isotropic, we can reconstruct the lensing potential ϕ with the so-called quadratic estimator (Hu & Okamoto 2002; Okamoto & Hu 2003). The lensing potential is linked to the convergence field κ_{CMB} by

$$\kappa_{\text{CMB}} = -\frac{1}{2}\Delta\phi \,. \qquad (11)$$

This convergence field is directly proportional to the surface mass density along the line of sight. The CMB lensing is as such an unbiased estimation of the distribution of mass. However it is an integrated estimation, whereas galaxy surveys can enable tomographic analyses thanks to redshift measurements.

The CMB lensing has been characterised by the *Planck* CMB survey (Planck Collaboration et al. 2020b), and by the ACTPol (Sherwin et al. 2017), SPT-SZ (Omori et al. 2017), and SPTpol (Wu et al. 2019) collaborations. Next-generation CMB surveys such as the Simons Observatory or CMB-S4 will increase the signal-to-noise ratios at all ℓ by almost one and two orders of magnitude, respectively. These new experiments will make the CMB lensing a sensitive probe of the dark matter distribution, and via cross-correlation studies it will be crucial to constraining the growth rate of the structure, the neutrino masses, or the level of primordial non-Gaussianities during the inflationary epoch.

3.4. Angular power spectra

Our statistical tools to test cosmological models are the angular two-point power spectra C_ℓ performed over the three fields defined in Sects. 3.1, 3.2, and 3.3. Assuming that the galaxy bias and the growth factors are scale independent, one can show that our (cross- and auto-) angular power spectra can be expressed as the convolution of two kernels $\Delta_\ell^{\text{A}}(k)$ and $\Delta_\ell^{\text{B}}(k)$, correspondingly for the fields A and B (see, e.g. Huterer et al. 2001):

$$C_\ell^{\text{A,B}} = \frac{2}{\pi} \int dk \, k^2 \, P(k) \, \Delta_\ell^{\text{A}}(k) \, \Delta_\ell^{\text{B}}(k), \qquad (12)$$

where $P(k)$ is the linear 3D matter power spectrum at $z = 0$, which is a function of the wave number k.

To obtain the theoretical prediction of our angular power spectra, we started from the 2D fields defined in Eqs. 7 and 10. The velocity field is related to the matter density contrast field via the linearised continuity equation $\partial\delta_{\text{m}}^{\text{3D}}/\partial t + \nabla\mathbf{v}/a = 0$, with $a(z)$ being the cosmological scale factor, $a = 1/(1+z)$. We introduce the following linear growth rate:

$$f = \frac{d\ln D}{d\ln a} = -(1+z)\frac{1}{D(z)}\frac{dD}{dz} \,. \qquad (13)$$

We assume $f(z) = \Omega_{\text{m}}(z)^\gamma$, with $\gamma = 0.55$ (Lahav et al. 1991; Linder 2005). The growth factor $D(z)$ is computed by integrating the growth rate $f(z)$.

One can show that the angular galaxy clustering kernel is the sum of two terms, one arising from the density of galaxies and the other from the peculiar line of sight velocities, $\Delta_\ell^g = \Delta_\ell^g|_\delta + \Delta_\ell^g|_v$ (see e.g. Padmanabhan et al. 2007):

$$\Delta_\ell^{g,i}|_\delta(k) = \frac{1}{N_g^i}\int_{z=0}^{\infty} dV_\Omega \, \bar{n}_g(z) \, W_i(z) \, b_g(z) \, D(z) \, j_\ell(k\,r(z)), \qquad (14)$$

$$\Delta_\ell^{g,i}|_v(k) = \frac{1}{N_g^i}\int_{z=0}^{\infty} dV_\Omega \, \bar{n}_g(z) \, H(z) \, f(z) \, D(z) \, \frac{dW_i}{dz}\frac{j_\ell'(k\,r(z))}{k} \,, \qquad (15)$$
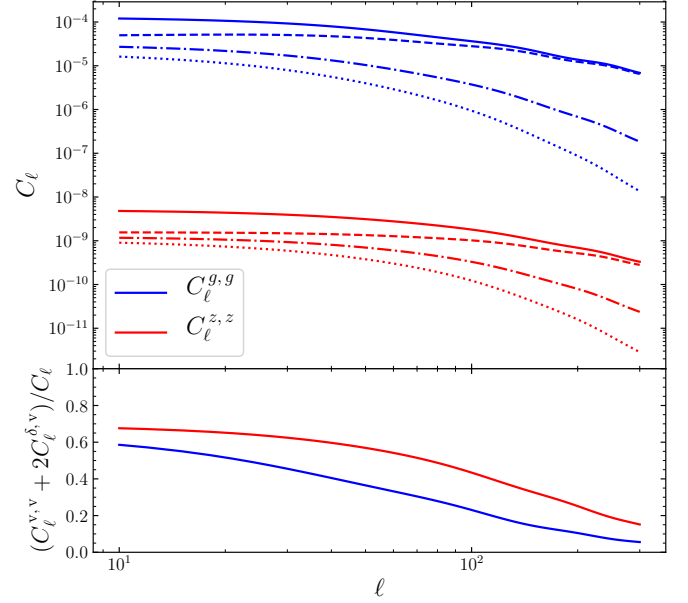

Fig. 2: *Top panel*: Power spectra of angular galaxy clustering (δ_g, in blue) and ARF (δ_z, in red), for a Gaussian redshift bin taken in a DESI-like survey. The bin is centred on $z_i = 0.75$ and has a standard deviation of $\sigma_z = 0.01$. The dashed line shows the term coming from the density kernel $C_\ell^{\delta,\delta}$, the dotted line shows the part coming from the velocity kernel $C_\ell^{v,v}$, and the dot-dashed line shows the cross term $C_\ell^{\delta,v}$. The total C_ℓ power spectra (plain lines) correspond to the sum $C_\ell = C_\ell^{\delta,\delta} + 2\,C_\ell^{\delta,v} + C_\ell^{v,v}$. *Bottom panel*: Velocity dependence ratio in the power spectrum ($C_\ell^{v,v} + 2\,C_\ell^{\delta,v}$) over the complete power spectrum, for the angular galaxy clustering (blue line) and for the ARF (red line). This figure shows that ARF are more sensitive to the peculiar velocity of galaxies than angular galaxy clustering, for the same redshift shell.

where $j_\ell(x)$ is the spherical Bessel function of order ℓ, and $j_\ell'(x)$ is its derivative $j_\ell'(x) \equiv d j_\ell/dx$.

One can thus write the power spectrum as the sum of the contributions from the density and from the velocity kernels $C_\ell = C_\ell^{\delta,\delta} + 2\,C_\ell^{\delta,v} + C_\ell^{v,v}$.

The ARF kernel can also be separated into two kernels:

$$\Delta_\ell^{z,i}|_\delta(k) = \frac{1}{N_g^i}\int_{z=0}^{\infty} dV_\Omega \, \bar{n}_g(z) \, W_i(z) \, b_g(z) \, D(z) \, (z - \bar{z}) \, j_\ell(k\,r(z)) \,, \qquad (16)$$

$$\Delta_\ell^{z,i}|_v(k) = \frac{1}{N_g^i}\int_{z=0}^{\infty} dV_\Omega \, \bar{n}_g(z) \, H(z) \, f(z) \, D(z) \, W_i(z)$$
$$\times \left[1 + (z - \bar{z})\frac{d\ln W_i}{dz}\right]\frac{j_\ell'(k\,r(z))}{k} \,. \qquad (17)$$

The kernel function of the CMB lensing convergence field is given by

$$\Delta_\ell^\kappa(k) = \frac{3\Omega_{\text{m,0}}}{2}\left(\frac{H_0}{c}\right)^2\int_{r=0}^{r_*} dr \, \frac{r}{a(r)}\frac{r_* - r}{r_*} D(z(r)) \, j_\ell(k\,r), \qquad (18)$$

where r_* the comoving distance from the observer to the last scattering surface, and a is the cosmological scale factor.

The top panel of Fig. 2 shows the angular power spectra of the angular galaxy clustering and ARF for a Gaussian selection

function of width $\sigma_z = 0.01$ centred on $z_i = 0.75$ in a DESI-like survey. In the same figure, we show the terms arising from the density fluctuation kernel and the peculiar velocity kernel (c.f. Eqs. 14 to 17). We can see that the peculiar velocity term is relatively more important (compared to the total power spectrum) in the ARF power spectrum than in the angular galaxy clustering power spectrum. To better illustrate this fact, in the bottom panel of Fig. 2 we show the ratio of the velocity part of the power spectrum (which is the sum $C_\ell^{v,v} + 2\,C_\ell^{\delta,v}$) over the total power spectrum for both angular galaxy clustering and ARF. For both fields, the peculiar velocity contribution dominates at low ℓ, while it vanishes to zero for $\ell > 300$. At $\ell = 10$, the velocity-dependent part in the power spectrum represents around 67 % of the total contribution for $C_\ell^{z,z}$, while it represents only 58 % of $C_\ell^{g,g}$. The difference between the two is even more visible at $\ell = 60$, where the velocity contribution represents 55 % of $C_\ell^{z,z}$ and only 35 % of $C_\ell^{g,g}$.

This difference is caused by the intrinsically different nature of the angular galaxy clustering and ARF transfer functions: angular galaxy clustering is sensitive to the average of density and velocity under the Gaussian shell, whereas ARF is sensitive to radial derivatives of those fields. For narrow shells, this makes both fields practically uncorrelated (HMCMA), and given the ratio comparison showed in Fig. 2, one would expect ARF to be more sensitive than angular galaxy clustering to cosmological parameters impacting peculiar velocities.

4. Signal-to-noise forecasts

We forecast the expected signal-to-noise ratio for different combinations of observables. Our data vector $\boldsymbol{D}(\ell)$ contains the auto- and cross-power spectra between the different observables and between the redshift bins. In order to compare several combinations of probes, we define the following data vectors:

$$\boldsymbol{D}_g(\ell) = \left(C_l^{g_i, g_j} \right) , \tag{19}$$

$$\boldsymbol{D}_z(\ell) = \left(C_l^{z_i, z_j} \right) ,$$

$$\boldsymbol{D}_{g,z}(\ell) = \left(C_l^{g_i, g_j}, C_l^{g_i, z_j}, C_l^{z_i, z_j} \right) ,$$

$$\boldsymbol{D}_{g,\kappa_{CMB}}(\ell) = \left(C_l^{g_i, g_j}, C_l^{g_i, \kappa_{CMB}}, C_l^{\kappa_{CMB}, \kappa_{CMB}} \right) ,$$

$$\boldsymbol{D}_{g,z,\kappa_{CMB}}(\ell) = \left(C_l^{g_i, g_j}, C_l^{g_i, z_j}, C_l^{g_i, \kappa_{CMB}}, C_l^{z_i, z_j}, \right.$$
$$\left. C_l^{z_i, \kappa_{CMB}}, C_l^{\kappa_{CMB}, \kappa_{CMB}} \right), \tag{20}$$

where i and j are indexes running over the redshift bins. We performed a tomographic analysis with 20 redshift bins, thus the data vectors containing only the auto-spectra of angular galaxy clustering and ARF ($\boldsymbol{D}_g$ and $\boldsymbol{D}_z$) contain 210 C_ℓ each. The data vector containing the cross-correlation $\boldsymbol{D}_{g,z}$ has 820 C_ℓ and the longest data vector $\boldsymbol{D}_{g,z,\kappa_{CMB}}$ contains 861 C_ℓ.

In Fig. 3, we display the correlation matrix for the $\boldsymbol{D}_{g,z,\kappa_{CMB}}(\ell = 10)$ data vector. We clearly see that, in the same redshift bin, angular galaxy clustering and ARF are practically un-correlated (diagonal terms of the top-left and lower-right blocks close to zero), but that there is some degree of anti-correlation in neighbouring redshift bins. We can also observe that the CMB lensing field is almost uncorrelated with the ARF.

We assume that there is no correlation between different multipoles and that the covariance between the probes is totally captured by a Gaussian covariance. This assumption is exact on large (linear) scales and if the survey covers the full sky. With
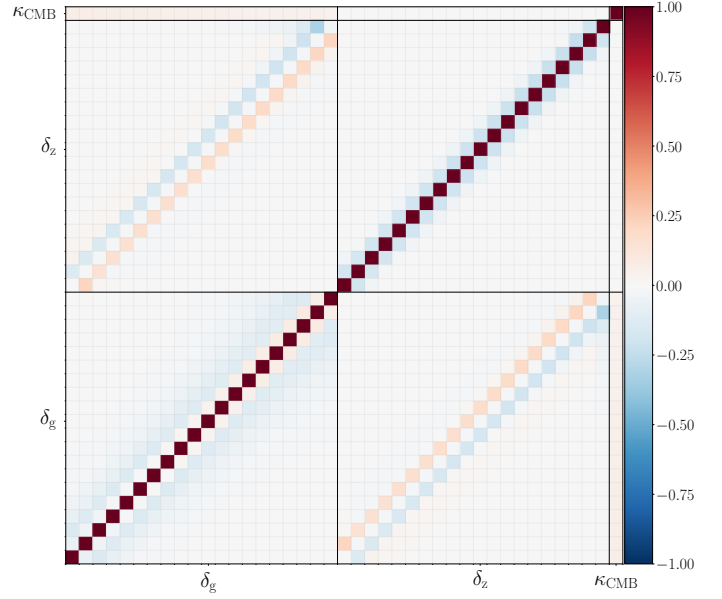

Fig. 3: Correlation matrix between our observables for the 20 redshift bins in an *Euclid*-like survey, at $\ell = 10$. This matrix corresponds to the $\boldsymbol{D}_{g,z,\kappa_{CMB}}(\ell = 10)$ data vector. The value in each pixel corresponds to $C_\ell^{A,B} / \sqrt{C_\ell^{A,A} C_\ell^{B,B}}$. All the data vectors considered in Eqs. 19 to 20 are a subset of this matrix. We see that there is no correlation between δ_g and δ_z inside the same redshift bin (diagonals of the upper-left and lower-right blocks), and that there are opposite and positive correlations for neighbouring bins.

regard to real data, the footprint of the survey and the presence of masked area will create correlations between multipoles. We invite the reader to consult, for example, Krause & Eifler (2017) or Lacasa (2018) for the inclusion of the higher order (non-Gaussian) terms in the covariance matrix. In this work, we neglect these effects.

The signal-to-noise ratios of our data vectors as a function of ℓ, taking into account all redshift bins and the correlations between them, are given by

$$S/N\left(\boldsymbol{D}(\ell)\right) = \sqrt{\boldsymbol{D}(\ell)^t\, \mathsf{Cov}_\ell^{-1}\, \boldsymbol{D}(\ell)} , \tag{21}$$

and the total signal-to-noise ratios are

$$S/N\left(\boldsymbol{D}\right) = \sqrt{\sum_{\ell=\ell_{min}}^{\ell_{max}} \left[SNR\left(\boldsymbol{D}(\ell)\right) \right]^2} . \tag{22}$$

Assuming that there is no correlation between different multipoles, we defined our Gaussian covariance matrix between our data vectors as in Hu & Jain (2004):

$$\mathsf{Cov}_\ell\left(C_\ell^{A,B}, C_\ell^{C,D} \right) = \frac{1}{(2\ell + 1)\,\Delta\ell\, f_{sky}}$$
$$\times \left[\left(C_\ell^{A,C} + \delta_{A,C}^K N_\ell^A \right)\left(C_\ell^{B,D} + \delta_{B,D}^K N_\ell^B \right) \right.$$
$$\left. + \left(C_\ell^{A,D} + \delta_{A,D}^K N_\ell^A \right)\left(C_\ell^{B,C} + \delta_{B,C}^K N_\ell^B \right) \right] , \tag{23}$$

with A, B, C, D being the observables $\{ g_i, z_j, \kappa_{CMB} \}$, $\Delta\ell$ the width of the multipole bin, $\delta_{x,y}^K$ the Kronecker delta, N_ℓ the